



Disturbed State constitutive modeling of two Pleistocene tills

S.M. Sane^a, C.S. Desai^a, J.W. Jenson^{b,*}, D.N. Contractor^a, A.E. Carlson^{c,1}, P.U. Clark^c

^aDepartment of Civil Engineering and Engineering Mechanics, University of Arizona, Tucson, AZ 85721, USA

^bWater and Environmental Research Institute of the Western Pacific, University of Guam, Mangilao, GU 96923, USA

^cDepartment of Geosciences, Oregon State University, Corvallis, OR 97331, USA

Received 15 June 2006; received in revised form 3 October 2007; accepted 8 October 2007

Abstract

The Disturbed State Concept (DSC) provides a general approach for constitutive modeling of deforming materials. Here, we briefly explain the DSC and present the results of laboratory tests on two regionally significant North American tills, along with the results of a numerical simulation to predict the behavior of one of the tills in an idealized physical system. Laboratory shear tests showed that plastic strain starts almost from the beginning of loading, and that failure and resulting motion begin at a critical disturbance, when about 85% of the mass has reached the fully adjusted or critical state. Specimens of both tills exhibited distributed strain, deforming into barrel shapes without visible shear planes. DSC parameters obtained from shear and creep tests were validated by comparing model predictions against test data used to find the parameters, as well as against data from independent tests. The DSC parameters from one of the tills were applied in a finite-element simulation to predict gravity-induced motion for a 5000-m long, 100-m thick slab of ice coupled to an underlying 1.5-m thick layer of till set on a 4° incline, with pore-water pressure in the till at 90% of the load. The simulation predicted that in the middle segment of the till layer (i.e., from $x = 2000$ to 3000 m) the induced (computed) shear stress, strain, and disturbance increase gradually with the applied shear stress. Induced shear stress peaks at ~ 60 kPa. The critical disturbance, at which failure occurs, is observed after the peak shear stress, at an induced shear stress of ~ 23 kPa and shear strain of ~ 0.75 in the till. Calculated horizontal displacement over the height of the entire till section at the applied shear stress of 65 kPa is ~ 4.5 m. We note that the numerical prediction of critical disturbance, when the displacement shows a sharp change in rate, compares very well with the occurrence of critical disturbance observed in the laboratory triaxial tests, when a sharp change in the rate of strain occurs. This implies that the failure and concomitant initiation of motion occur near the residual state, at large strains. In contrast to the Mohr–Coulomb model, which predicts failure and motion at very small (elastic) strain, the DSC thus predicts failure and initiation of motion after the till has undergone considerable (plastic) strain. These results suggest that subglacial till may be able to sustain stress in the vicinity of 20 kPa even after the motion begins. They also demonstrate the potential of the DSC to model not only local behavior, including potential “sticky spot” mechanisms, but also global behavior for soft-bedded ice.

© 2007 Elsevier Ltd. All rights reserved.

1. Introduction

Glacial ice moves by a combination of ice deformation and subglacial processes that include sliding, ploughing, and deformation of basal sediment. Although the mechanics of ice deformation is relatively well understood,

subglacial processes are complex, and their roles in ice sheet behavior have been subjects of ongoing research and vigorous debate for the past two decades. In the mid-1980s, the discovery that the West Antarctic ice streams rested on water-saturated, fine-grained sediments stimulated interest in the mechanical properties of subglacial tills and the processes by which they might influence ice sheet behavior (Alley et al., 1986; Blankenship et al., 1986). Models assuming that ice movement is controlled by viscous-style till behavior (e.g., Alley et al., 1987a,b; Alley, 1989a,b; MacAyeal, 1989; Jenson et al., 1996) were thus developed to explore ice sheet behavior and its implications for global climate and sea level. Extant interpretations of the

*Corresponding author. Tel.: +1 671 735 2689; fax: +1 671 734 8890.

E-mail addresses: shantanu@email.arizona.edu (S.M. Sane), csdesai@engr.arizona.edu (C.S. Desai), jjenson@uog.edu (J.W. Jenson), contact@dakotacom.net (D.N. Contractor), acarlson@geology.wisc.edu (A.E. Carlson), clarkp@onid.orst.edu (P.U. Clark).

¹Now at Department of Geology and Geophysics, University of Wisconsin-Madison, 1215 W Dayton Street, Madison, WI 53706, USA.

sediment record (e.g., Alley, 1991; Johnson and Hansel, 1999) lent support to the assumption of distributed strain and viscous-style deformation in subglacial till. Geophysical models of global phenomena involving ice sheet growth and decay (e.g., DeConto and Pollard, 2003; Tarasov and Peltier, 2004) continue to rely on such models of till behavior for simulating global ice sheet behavior.

In the meantime, field and laboratory experiments have indicated that such models might be too simple. Laboratory experiments by Kamb (1991) on sediment recovered from beneath Ice Stream B (now Whillans Ice Stream) showed residual strengths much too weak to support the driving stresses, suggesting that “sticky spots” of unknown character must occur to resist the balance of the basal shear stress. A subsequent field experiment on Columbia Glacier, Alaska, by Humphrey et al. (1993) showed compelling evidence for distributed viscous-style deformation in a basal till layer. However, it also indicated that sediment strength or viscosity was insufficient to resist glacier flow. Other laboratory and field experiments (e.g., Iverson et al., 1998, 1999; Iverson, 1999; Tulaczyk et al., 2000a,b; Kavanaugh and Clarke, 2006) produced results consistent with simple Mohr–Coulomb rheology, and exhibiting failure planes with insufficient strength to account for stable fast-ice motion. (See Clarke (2005) for a comprehensive summary of the work to date and the current state of the debate.)

Attempts to reconcile these disparate results include Hindmarsh’s (1997) suggestion that multiple small areas of such weak tills might fail, move as slurries, reconsolidate, and fail again, with the net effect being essentially viscous deformation with sufficient overall strength to support stable fast ice flow. Others have proposed that strain might be distributed vertically through layers of Coulomb-plastic materials by dilatant hardening (Iverson et al., 1998), pore-pressure diffusion (Tulaczyk, 1999), or differential slippage from fluctuations in effective normal stress resulting from the failure of grain bridges (Iverson and Iverson, 2001). Piotrowski et al. (2004) proposed that soft beds under warm-based glaciers can be envisaged as a mosaic in which deformation is limited to centimeter-scale depths within transient patches, and that basal sliding probably contributes more to ice motion than does bed deformation (Piotrowski et al., 2001). Fischer and Clarke (1999) have suggested that transient deforming patches of till may account for sticky spots, thus serving to stabilize rather than mobilize glacial ice. The mechanisms by which bed deformation might influence ice motion and the contributions that it might thus make to ice sheet behavior therefore remain uncertain. What does seem certain, however, is that more than a single type of behavior or mechanism must be involved.

We propose that progress in understanding the behavior of subglacial till and its contributions to ice sheet behavior can be facilitated by the application of a general constitutive model that can account for and integrate the various behaviors observed in granular materials, including

their interaction with material interfaces (e.g., sliding). Such a model should be able to account for both local and global behaviors, and would incorporate the classical models as special cases. Interface behavior, including sliding, would also be seen as an integral and related process rather than as separate and different from sediment deformation. We note here that the focus of this study was the potential effect of the deforming till on the glacial motion; the effect of the relative motion between the till and the overlying ice will be the subject of future research.

Clarke (1987) first proposed such a general framework for the behavior of till based on the continuum theory of mixtures. Clarke’s model treated till as a mixture of water, clasts, and fined-grained matrix, and incorporated processes of diffusive water flow, fine-grained sediment transport, consolidation, shear deformation, and comminution. Numerical solutions of the state equations predicted system response to changes in five variables. This type of approach, however, has since been largely neglected as research has focused on collecting and interpreting observations from laboratory and field studies.

In this paper, we present the results of tests conducted to evaluate the mechanical properties of two Pleistocene tills using the Disturbed State Concept (DSC) (Desai, 1974, 2001; Desai and Ma, 1992; Desai and Toth, 1996). The DSC is a general, unified approach that describes the self-adjustment or self-organization in deforming material from its initial state toward the ultimate (failure or collapse) end state, as influenced by such factors as the stress state, stress path, volume change including dilation, microcracking, and microstructural instabilities. As with Clarke’s (1987) approach, the DSC incorporates established classical continuum models along with the fully adjusted (FA) or classical critical state model (e.g., Roscoe et al., 1958), thus accommodating a range of behaviors in a single, integrated framework.

The DSC model had its origin in a simple model for over-consolidated soil in which the behavior was decomposed into that of the same material in the normally consolidated state and that due to the influence of over-consolidation (Desai, 1974). The DSC has since been developed and generalized for application to a wide range of materials including soils, rocks, concrete, ceramics, asphalt, metal alloys, and silicon (cf., Desai and Ma, 1992; El Sakhway and Edil, 1996; Desai et al., 1997b, 1998; Geiser et al., 1999; Pal and Wathugala, 1999; Varadarajan et al., 1999; Fakharian and Evgin, 2000; Prochazka and Trckova, 2000; Varadarajan and Sharma, 2000; Vulliet and Laloui, 2000). Its utility for modeling sediment deformation has been well established by its remarkably successful application to an instrumented creeping landslide in Villarbeney, Switzerland (Desai et al., 1995).

We note here that we intend to apply the DSC to the study of sliding in future research. The purpose of the study reported in this paper, however, is to isolate and characterize the potential contribution of subglacial sediment deformation to ice motion. After presenting a brief

explanation of the DSC, we report the results of our laboratory tests and the application of the parameters obtained from them to a numerical simulation of an idealized coupled ice–sediment system.

2. Disturbed state model

This section summarizes the fundamental concepts, the derivation of the governing equation, and the models by which the various deformational behaviors are incorporated in the DSC. For comprehensive explanations of the theory, methodologies, and applications of the DSC, the reader is referred to Desai (2001).

2.1. Fundamental concepts: the reference states and the disturbance function

The fundamental idea underlying the DSC is the well-known tenet that when forces or other external environmental factors acting on a material body change, the material begins adjusting from its existing state toward a new equilibrium state. Complete adjustment of the entire mass may never be fully reached or may not be measurable in practice. Nevertheless, the early behavior of the material can be observed and measured, and the ideal final state can be inferred from trends exhibited during deformation.

The fundamental difference between the DSC and the classical constitutive models is that the DSC accommodates the fact that deforming material is usually not continuous. Rather, it recognizes that the deforming material, at every stage, is composed of an evolving combination of continuous and discontinuous parts. The overall behavior can be quantified in terms of the relative contributions of the continuous and discontinuous portions. The framework of the DSC thus allows identification of threshold states, including the transition from compressive to dilative volume change, peak stress, and unstable states such as failure and liquefaction (Desai, 2000). According to this model, the failure or collapse resulting in movements is defined not simply in terms of the peak

stress, but in terms of the combination of stress, strain and other variables such as void ratio, volumetric strain, accumulated plastic strain or disturbance. The DSC also allows for stiffening or “healing” conditions. Finally, it accommodates the classical models as special cases, imparting the concept a hierarchical property.

2.1.1. The relative intact (RI) state

The RI state is defined as the intact state relative to the subsequent or modified state. The RI behavior can be characterized using models based on continuum theories such as elasticity, plasticity, and viscoplasticity (Desai, 2001).

2.1.2. The FA state

During deformation, the material undergoes microstructural transformations or adjustments due to processes such as microcracking and relative particle motions. Hence, the overall material cannot be considered as continuous; rather it is a mixture of continuous and discontinuous parts. As a material element deforms, the self-adjustment of the material particles forms disturbed zones that are distributed throughout the material (Fig. 1). These zones coalesce, and in the limit the entire material element approaches the FA state. The FA zones interact with the adjacent RI zones, and as they accumulate, the behavior of the material body diverges from that predicted by the continuum (RI) model and approaches the *asymptotic* or *ultimate FA state*, denoted as FA_{∞} (Fig. 2). A material can be said to fail when it has accumulated a critical volume of FA zones. Some vestiges of the original RI material may persist, but eventually they become insufficient to have measurable effect on the behavior of the material, which is thus dominated by the FA state. The ultimate FA state can be predicted approximately from laboratory tests, but is seldom measured in laboratory or natural systems.

A number of models can be used to characterize the FA state. In general, FA material can behave as a *constrained liquid*, i.e., support hydrostatic stress but not shear stress, or as a *constrained liquid–solid*, i.e., support a given shear

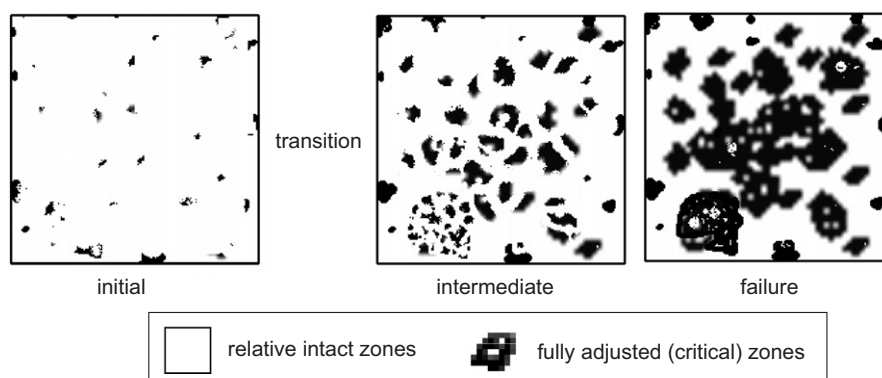


Fig. 1. Schematic diagram of the development of fully adjusted (FA) clusters in a deforming material element as it evolves from the relative intact (RI) state to failure.

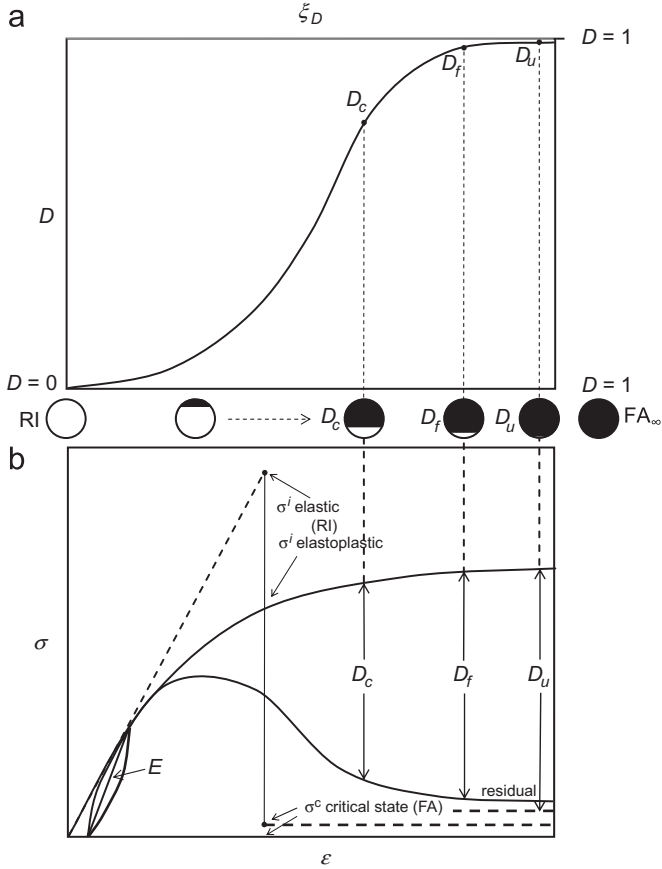


Fig. 2. Schematic diagram of the stress–strain curve and corresponding disturbance curve for a continuously yielding material: (a) the critical disturbance, D_c , which signals the onset and propagation of collapse, occurs before the defined failure disturbance, D_f , at which the behavior of the material element is dominated by the FA portion. The ultimate, or residual disturbance D_u , is the asymptotic or limiting value, which is rarely reached in laboratory experiments. The residual state thus defined reflects the survival, and even the persistence, of a residual but insignificant and inconsequential RI portion of the material element. Note that the disturbance function is of the same general shape as that exhibited in decay and growth in many other natural systems; (b) schematic diagram of the evolution of the stress–strain behavior and its relationship to the disturbance. As the deforming material element transforms from the RI to FA state, the ratio of the FA mass, M^c , to the total mass, M (see Eq. (1)) passes through threshold transitions such as contractive to dilative volume changes, peak, and residual. The other quantities and relationships illustrated on the graph are explained in Section 2 of the text.

stress for a given hydrostatic stress. In soil mechanics, the latter behavior is referred to as a *critical state* response. For granular materials such as till, the critical state model is appropriate for characterizing the FA response. Critical state theory is mature and well documented in the geotechnical literature (Roscoe et al., 1958; Muir-Wood, 1990). Established techniques for evaluating critical state parameters can thus be employed to characterize the FA state.

2.1.3. The disturbance function

The relative contributions of the RI and FA portions to the overall behavior of a deforming material can be

expressed through the disturbance function, D , which reflects the proportion of the total mass that has transitioned to the FA state (Fig. 2). Thus

$$D \equiv \frac{M^c}{M}, \tag{1}$$

where M is the total mass of the material element, and M^c is the mass in the critical, FA state. Initially, $D = 0$. At the end state, i.e., FA_∞ , $D = 1$. Because the mass in the FA state cannot usually be measured directly, D is normally evaluated in terms of correlative phenomena that can be measured in laboratory experiments, such as accumulated plastic stain or work. A useful model for disturbance is

$$D = D_u[1 - \exp(-A\xi_D^Z)], \tag{2}$$

where ξ_D is the deviatoric plastic strain trajectory (also see Eq. (7e) below), and A , Z , and D_u are material parameters.

2.2. Derivation of the governing equation

Based on the equilibrium of forces, the stress components within a deforming material element (superscript a) are the sum of the stress components borne by the RI portion (superscript i) and those borne by the FA portion (superscript c):

$$\sigma_{ij}^a = (1 - D)\sigma_{ij}^i + D\sigma_{ij}^c. \tag{3}$$

The incremental forms of Eq. (3) are

$$d\sigma_{ij}^a = (1 - D)d\sigma_{ij}^i + Dd\sigma_{ij}^c + dD(\sigma_{ij}^c - \sigma_{ij}^i) \tag{4}$$

or

$$d\sigma_{ij}^a = (1 - D)C_{ijkl}^i d\epsilon_{kl}^i + DC_{ijkl}^c d\epsilon_{kl}^c + dD(\sigma_{ij}^c - \sigma_{ij}^i), \tag{5}$$

where C_{ijkl}^i and C_{ijkl}^c are the respective constitutive tensors for the RI and FA states, and ϵ_{ij} is the strain tensor. Note that when there is no disturbance, i.e., when $D = 0$, the RI term is the only non-zero term, and Eq. (5) reduces to the continuum model. As D approaches 1, however, the RI term vanishes as the FA state comes to dominate (Fig. 2). Application of the DSC thus consists, first, of identifying an appropriate function for the disturbance, D , along with appropriate constitutive models for the RI and FA states and, second, of evaluating the parameters for the disturbance and constitutive relations.

2.3. Reference states

2.3.1. RI behavior

The RI state defined by C_{ijkl}^i can be characterized by elastic and elastoplastic continuum models. The incremental constitutive tensor, C_{ijkl}^i , can thus be given by

$$d\sigma_{ij}^i = C_{ijkl}^{ep} d\epsilon_{kl}^i \tag{6a}$$

and

$$C_{ijkl}^{ep} = C_{ijkl}^e - C_{ijkl}^p, \tag{6b}$$

where C_{ijkl}^{ep} is the elastoplastic tensor and C_{ijkl}^e (see Section 2.3.1.1) and C_{ijkl}^p (see Section 2.3.1.2) are the elastic and plastic components, respectively.

2.3.1.1. Elastic behavior. Here the elasticity tensor, C_{ijkl}^e (Eq. (6b)) is defined based on elastic constants such as Young's modulus, E , and Poisson's ratio, ν . In general, these are obtained from the slopes of the unloading response (see Fig. 2).

2.3.1.2. Plastic behavior: the hierarchical single-surface (HISS) model. In the present work, the HISS plasticity model (Desai, 2001) has been used for characterizing the plastic component of the RI behavior. The plasticity tensor, C_{ijkl}^p (Eq. (6b)) is defined from the HISS plasticity model (Fig. 3), in which the general yield function, F , is given by

$$F = \bar{J}_{2D} - (\alpha \bar{J}_1^n + \gamma J_1^2)(1 - \beta S_r)^{-0.5} = 0, \quad (7a)$$

where J_{2D} and J_1 are the second invariant of the deviatoric stress tensor and the first invariant of σ_{ij} , respectively. The over-bar denotes the invariants are non-dimensionalized with respect to atmospheric pressure, p_a . Thus, $\bar{J}_{2D} = J_{2D}/p_a$ and $\bar{J}_1 = (J_1 + 3R)/p_a$, in which the parameter, R , is computed from the intercept on the J_1 -axis for $\sqrt{J_{2D}} = 0$. It is thus related to the cohesive strength, \bar{c} , the intercept of the ultimate yield surface on the $\sqrt{J_{2D}}$ axis when $J_1 = 0$, by

$$R = \frac{1}{3}\bar{c}\gamma^{1/2}. \quad (7b)$$

The parameters γ and β are associated with the slope of the ultimate yield envelope (Fig. 3) and the shape of the yield surface in σ_1 - σ_2 - σ_3 space, respectively. The exponent, n , is associated with contractive to dilative volume change. The parameter, S_r , is the stress ratio, $\frac{1}{2}\sqrt{27}J_{3D}J_{2D}^{-3/2}$, in which J_{3D} is the third invariant of the deviatoric stress tensor. The coefficient, α , is the continuous

hardening (yielding) or growth function given by

$$\alpha = a_1/\xi^{\eta_1}, \quad (7c)$$

where a_1 and η_1 are hardening parameters, and ξ is the total plastic strain trajectory,

$$\xi = \int (d\epsilon_{ij}^p dE_{ij}^p)^{1/2}, \quad (7d)$$

in which ϵ_{ij}^p is the plastic strain tensor and ξ is the sum of the deviatoric and volumetric plastic strains:

$$\xi = \xi_D + \xi_v = \int (dE_{ij}^p dE_{ij}^p)^{1/2} + \frac{1}{\sqrt{3}}|e_{ii}^p|, \quad (7e)$$

where E_{ij}^p is the deviatoric plastic strain tensor, $\epsilon_{ij}^p - (1/3)\epsilon_{kk}\delta_{ij}$, and $e_{ii}^p = \epsilon_{ii}^p$ is the volumetric plastic strain.

The ultimate yield envelope defines the asymptotic stress states, i.e., the limiting asymptotic values of stress exhibited in the stress-strain curves under different confining pressures. The failure or peak stress states of the classical models thus plot below the ultimate line, or may coincide with it.

2.3.1.3. Creep behavior: the multicomponent DSC (MDSC) overlay model. The MDSC model (Fig. 4) includes elastic (e), viscoelastic (ve), elasto-viscoplastic (evp), and viscoelastic-viscoplastic (vevp) creep responses in a hierarchical manner² (Desai, 2001). In the Perzyna (evp) model, the total strain rate is decomposed into an elastic component and a viscoplastic component:

$$\dot{\epsilon}_{ij} = \dot{\epsilon}_{ij}^e + \dot{\epsilon}_{ij}^{vp}, \quad (8a)$$

where the superscripts e and vp denote the elastic and viscoplastic strain rate tensors, respectively. The viscoplastic strain rate, $\dot{\epsilon}_{ij}^{vp}$, is given by

$$\dot{\epsilon}_{ij}^{vp} = \Gamma \langle \phi \rangle \frac{\partial F}{\partial \sigma_{ij}}, \quad (8b)$$

where Γ is the fluidity parameter, F is the yield function, σ_{ij} is the stress tensor, and ϕ is the flow function, given by

$$\phi = (F/F_0)^N, \quad (8c)$$

in which N is a material parameter, and F_0 is the reference value of the yield function. The angle bracket around ϕ denotes a switch-on/switch-off operator such that

$$\begin{aligned} \langle \phi(F/F_0) \rangle &= \phi(F/F_0) \quad \text{if } F/F_0 > 0 \quad \text{and} \\ \langle \phi(F/F_0) \rangle &= 0 \quad \text{if } F/F_0 \leq 0. \end{aligned} \quad (8d)$$

Parameters Γ and N for the evp model are determined from laboratory creep tests. The parameters for the vevp model can also be determined from creep tests as described in Desai (2001).

2.3.2. FA behavior

In the present work, the FA state is characterized using the critical state model (Roscoe et al., 1958; Desai, 2001) to

²The earlier overlay model (Pande et al., 1997) can be regarded as a special case of the MDSC.

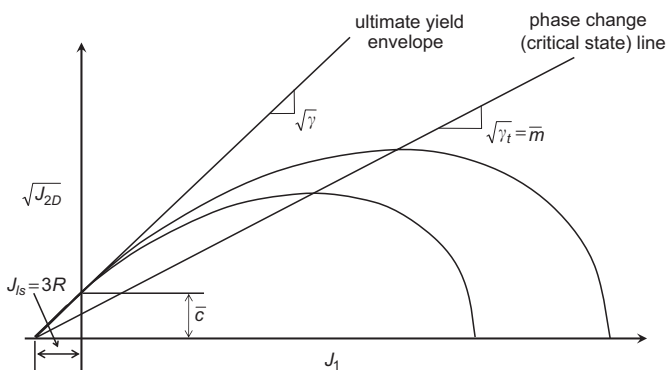


Fig. 3. Schematic diagram of the yield surface of the HISS plasticity model in $J_1^{1/2}$ - J_1 space. The ultimate yield envelope is obtained from the asymptotic stress, based on the peak stress in the stress-strain curves. The phase change (critical state) line intersects the apex of successive individual yield surfaces. See text for explanation of the parameters.

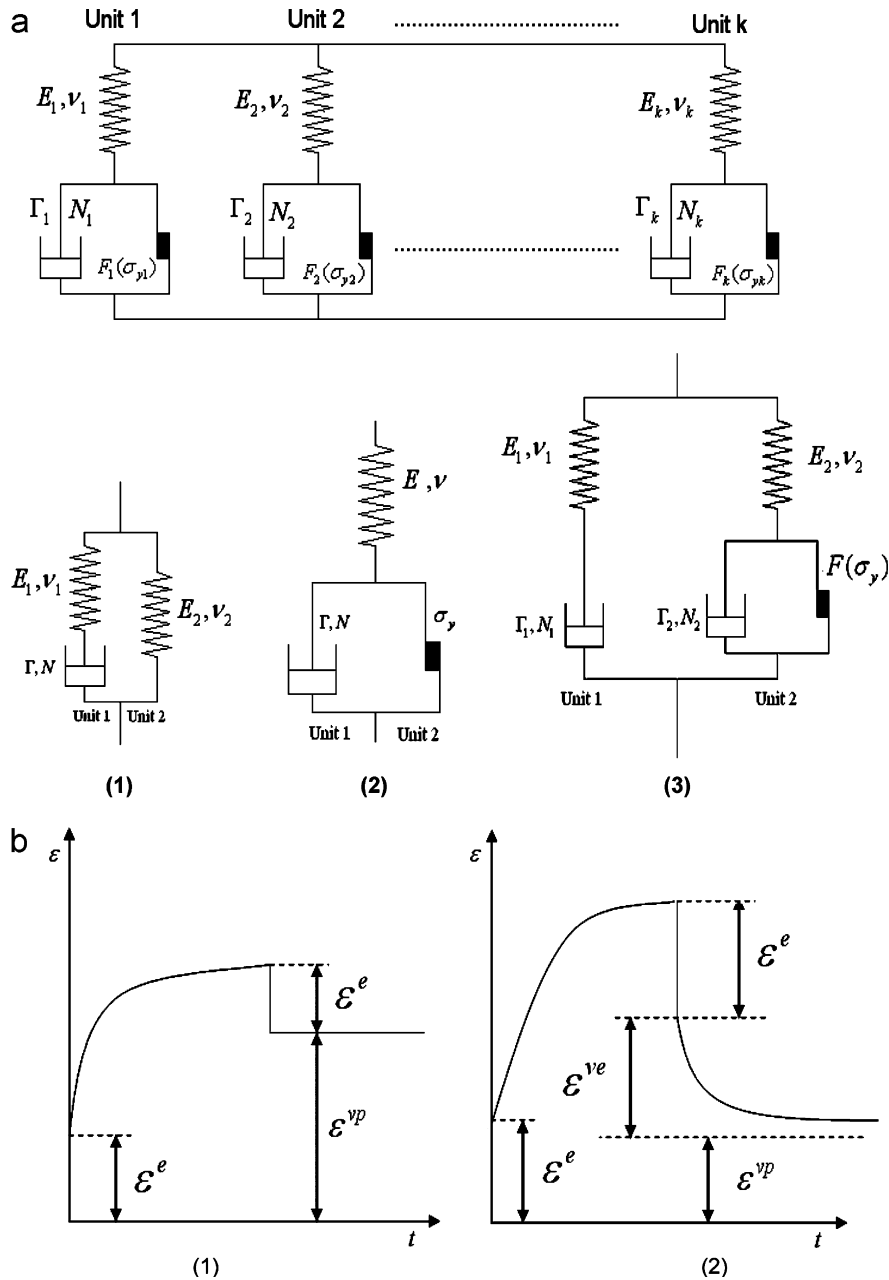


Fig. 4. (a) MDSC model and its specializations to: (1) viscoelastic (ve) model; (2) elastoviscoplastic (evp) or Perzyna model; and (3) viscoelastic-viscoplastic (vevp) model; (b) Creep responses for (1) the evp (Perzyna model) and (2) the vevp model. The spring element in the schematic (Fig. 4a(2)) represents the elastic part of the material response in the Perzyna model. An applied load causes an instantaneous elastic strain, ϵ^e , in the spring element (Fig. 4b(1)). The slider and the dashpot in Fig. 4a(2) represent the viscoplastic part of the behavior, and the applied load causes permanent strains due to the slider. Upon unloading, the elastic part of the strain, ϵ^e , is recovered instantaneously in the spring element, but the rest of the strain is retained permanently (ϵ^{vp}) (Fig. 4b(1)). In the vevp model (Fig. 4a(3), b(2)), when the applied load is removed, the elastic strain, ϵ^e , is recovered instantaneously in the spring elements, and the viscoelastic part of the strain, ϵ^{ve} , is recovered gradually in the dashpot (Fig. 4b(2)). The viscoplastic part stays permanently in the slider of Unit 2 (Fig. 4a(3)).

evaluate C_{ijkl}^c . Thus,

$$\sqrt{J_{2D}^c} = \bar{m} J_1^c, \quad (9)$$

$$e^c = e_0^c - \lambda \ln\left(\frac{1}{3} J_1^c / p_a\right), \quad (10)$$

where e^c is the void ratio at the critical state, \bar{m} is evaluated from the slope of the critical state line (Fig. 5a), e_0^c is the initial void ratio corresponding to $J_1^c = 3p_a$, and λ is the

slope of the consolidation line on a plot of e vs. $\ln\left(\frac{1}{3} J_1^c / p_a\right)$ (Fig. 5b).

3. Testing and methods

This section summarizes the testing program, its results, and their validation. Procedures for evaluating the DSC parameters are well established and described in detail

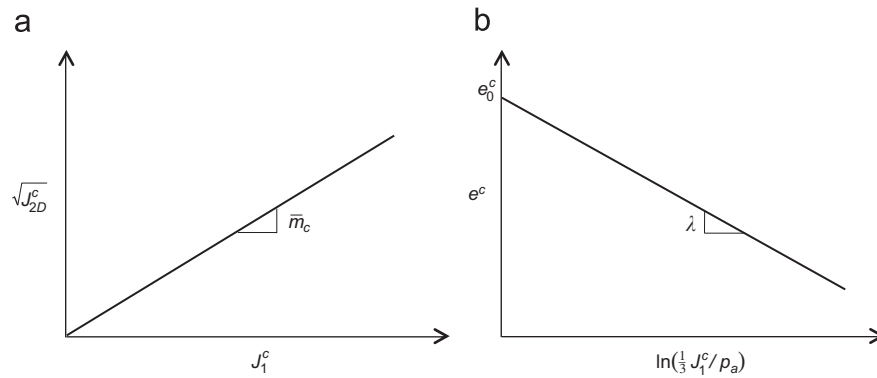
Fig. 5. Evaluation of critical state parameters: (a) \bar{m} and (b) λ .

Table 1
Compositional analyses for two tills (from Carlson et al., 2004)

Till unit	Sand (%)	Standard deviation	Silt (%)	Standard deviation	Clay (%)	Standard deviation ^a	Gravel fraction (> 2 mm)
Tiskilwa	45	2	39	5	16	7	~6% ^b
Sky Pilot	17	2	57	7	26	5	~4% ^c

^aBased on 11 Tiskilwa Till samples and 8 Sky Pilot Till samples.

^bFrom Johnson and Hansel (1990), Wickham and Johnson (1981).

^cFrom Roy (1998).

elsewhere (Desai et al., 1986, 1997a; Desai and Toth, 1996; Desai, 2001).

3.1. The selected tills: compositional characteristics

The first of the tills selected for this study is the lower unit (D1) of the Tiskilwa Formation in northern Illinois, deposited by the Lake Michigan Lobe of the Laurentide Ice Sheet between ~21,500 and 19,000 yr BP (Hansel and Johnson, 1996). It is one of the most extensive till units in the Midwest (Wickham and Johnson, 1981), and is typical of the widespread “loamy” tills deposited along the southern Laurentide Ice Sheet margin (Wickham and Johnson, 1981; Mickelson et al., 1983). Its stratigraphy, composition, and history are well documented (Johnson and Hansel, 1990). The D1 unit (hereafter referred to in this paper as the Tiskilwa Till) is 5–6 m thick in the study area. Samples for testing were obtained at mid-section. The till has a consistently strong macro-fabric and the basal contact is gradational with the underlying sediment (Carlson et al., 2004).

The second till is the Sky Pilot Till of northern Manitoba (Klassen, 1986). The Sky Pilot Till was deposited across the Hudson and James Bay lowlands by southwesterly ice flow sometime between 25,000 and 12,000 yr BP (Klassen, 1986; Thorleifson et al., 1992), and is representative of the substrate underlying a large portion of the center of the ice sheet (Dredge and Nielsen, 1985; Nielsen et al., 1986; Thorleifson et al., 1992). The till is approximately 6 m thick

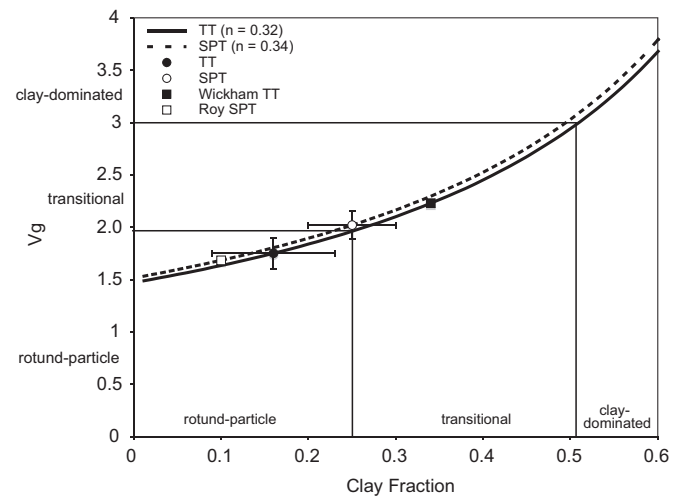


Fig. 6. Granular specific volume, v_g , vs. clay percent, at the initial saturated porosities for each of the tills examined in this study. $v_g \equiv 1 + (v_w + v_p)/v_r$, where v_w is the volume of the fluid phase, v_p is the volume of the low-friction platy particles, and v_r is the volume of the rotund particles plus high-friction platy particles (Lupini et al., 1981; Muir-Wood, 1990). The two curves plot close together because the initial porosities are similar: 0.32 (void ratio 0.477) for the Tiskilwa Till, and 0.34 (void ratio 0.52) for the Sky Pilot Till. Round symbols with error bars show the mean v_g values and standard deviations of the clay fractions for the samples examined in this study. For porosities ranging from 20% to 50% (not shown in this figure), v_g would range from 1.5 to 2.4 for the Tiskilwa Till and from 1.7 to 2.0 for the Sky Pilot Till. Compositions of the same till units reported by others (Wickham and Johnson, 1981; Johnson and Hansel, 1990; Roy, 1998), with the corresponding values of v_g , are also shown.

in the study area. Samples were obtained at mid-section. The Sky Pilot Till has a 1-m gradational contact with the underlying Long Spruce Till, which has a deformed contact with the underlying sediment. Macro-fabric is moderately strong and variable in strength throughout the section (Carlson et al., 2004).

Compositional analyses of our samples are shown in Table 1. Both tills plot as rotund-particle-dominated to transitional by the criteria of Lupini et al. (1981), Muir-Wood (1990), and Skempton (1985) (Fig. 6). Index properties obtained by standard tests (Lambe and Whitman, 1969) are shown in Table 2.

3.2. Tests and results

Tests were conducted on each of the two tills (Table 3) to evaluate the elastic, plastic, disturbance, and creep parameters for each till (Tables 4–6). Till samples were passed through a 2-mm sieve, moistened to saturation, and then pre-consolidated. Standard test specimens of 7-cm radius \times 14-cm length were extracted by Shelby tube.

Table 2
Index properties of the Tiskilwa and Sky Pilot Tills

Properties	Tiskilwa Till	Sky Pilot Till
Field moisture content (%)	17	16
Plasticity index (%)	16 \pm 2	18 \pm 2
Liquid limit (%)	22 \pm 2	20 \pm 2

Table 3
Triaxial tests for Tiskilwa and Sky Pilot Tills

Type of tests ^a	Number of tests		Confining pressure	Comments
	Tiskilwa	Sky Pilot		
Consolidated undrained (CTC)	10	8	$\sigma_3' = 20^b, 50^b, 100, 200, 300, 500$ kPa	Results of these tests are used to calculate the DSC model parameters
Consolidated undrained (CTC) (independent)	2	2	$\sigma_3' = 150, 400$ kPa (independent)	Results of these tests are not used for parameter calculation but are used for independent validations
Creep tests	11	11	$\sigma_3' = 100, 200, 400$ kPa	At each confining pressure, 4 tests are performed, respectively, at 20%, 40%, 60%, and 80% of the peak stresses (obtained from CTC tests). Results of these tests are used to obtain the parameters for the MDSC model
Creep tests (independent)	4	4	$\sigma_3' = 300$ kPa (independent)	These are similar to above tests, but results of these tests are not used for parameter calculation but rather are used for independent validations

^aNote: At least 2 unloading cycles before and after the peak stress are performed, except for the creep tests.

^bLow-confining-pressure test conducted using procedures described in Section 3.2 for Tiskilwa Till only.

Table 4
Elastic, plastic, critical state, creep and disturbance parameters for the Tiskilwa and Sky Pilot Tills

DSC state	Behavior	Parameter name	Symbol	Equation	Tiskilwa Till	Sky Pilot Till
Disturbance function	Disturbance	Reference disturbance	D_u	(2)	1	1
		Disturbance parameter	Z		2.68	1.00
		Disturbance parameter	A		20.20	5.50
Relative intact state	Elastic	Young's Modulus	E	(6b)	57,732 kPa	50,470 kPa
		Poisson's Ratio ^a	ν		0.45	0.45
	Plastic	Transition parameter	n	(7a)	3.60	6.85
		Ultimate parameter	β		0.36	0.52
		Ultimate parameter	γ		0.0178	0.0092
		Cohesive strength	\bar{c}	(7b)	6.79 kPa	16.67 kPa
	Creep	Hardening parameter	a_1	(7c)	2E-4	1.35E-7
		Hardening parameter	η_1		0.27	0.14
		Fluidity parameter	Γ	(8b)	See Tables 5 and 6 ^b	
		Flow exponent	N	(8c)		
Fully adjusted state	Critical state	Critical state line slope	\bar{m}	(9)	0.10	0.09
		Consolidation line slope	λ	(10)	0.21	0.16
		Reference void ratio	e_c^0		0.48	0.52

^aPoisson's ratio, ν , is taken to be 0.45 (less than 0.50) since the sample is fully saturated and is tested under undrained conditions.

^bCreep tests on the Tiskilwa Till (Pandey, 2005) were exploratory; the parameters obtained from them will be revised and reported later.

Table 5
Creep parameters for elasto-viscoplastic (evp) model: Sky Pilot Till

evp Creep parameters	Confining pressure ($\sigma_2 = \sigma_3$)		
	100 kPa	200 kPa	400 kPa
E (kPa)	41000	45000	58000
ν	0.45	0.45	0.45
Γ ($\text{kPa}^{-1} \text{min}^{-1}$)	5.5E-06	2.17E-07	3.4E-08
N	1.625	2.2	2.0

Table 6
Creep parameters for viscoelastic-viscoplastic (vevp) model: Sky Pilot Till

vevp creep parameters	Confining pressure ($\sigma_2 = \sigma_3$)		
	100 kPa	200 kPa	400 kPa
E_1 (kPa)	6666	24244	30000
E_2 (kPa)	42500	83333	63333
ν_1	0.45	0.45	0.45
ν_2	0.45	0.45	0.45
Γ_1 ($\text{kPa}^{-1} \text{min}^{-1}$)	1.45E-03	1.84E-03	4.24E-06
Γ_2 ($\text{kPa}^{-1} \text{min}^{-1}$)	0.006	0.006	0.006
N_1	2.275	4.0	1.4
N_2	1.625	2.2	2.0

Strain-controlled conventional triaxial compression (CTC) tests (Sane, 2007) were performed undrained with shear stress measured in response to displacement. For the creep tests (Pandey, 2005; Sane, 2007), displacement rate was measured in response to specified constant axial loads. A notable observation is that in all cases the test specimens deformed continuously, in barrel shapes (Fig. 7); shear planes were not observed.

Effective stresses at the base of modern ice streams have been observed to be very low, in the range of 10–50 kPa (Engelhardt et al., 1990; Engelhardt and Kamb, 1997; Kamb, 2001). However, in the laboratory it is very difficult to prepare a cylindrical sample that can stand its own weight at such low confining pressures. Even when it does, the sample may deform irregularly during loading, making it difficult to compute stress from the deforming diameter. We were nevertheless able to perform two successful low-confining stress tests on specimens of Tiskilwa Till, under $\sigma_3' = 20$ and 50 kPa, by freezing test specimens in molds, and then removing the molds and thawing the specimen in the test cell prior to consolidation. From Fig. 8, it can be seen that inclusion of the low-confining pressure tests does not significantly influence the Mohr–Coulomb envelopes, nor (by extension) the ultimate yield envelopes (Fig. 3). We also found that use of low-confining pressure tests do not influence the DSC/HISS parameters significantly (Sane, 2007).



Fig. 7. Photographs of CTC test samples: (a) before the test; and (b), (c), (d) after test; (b) for Sky Pilot; and (c) and (d) for Tiskilwa Till.

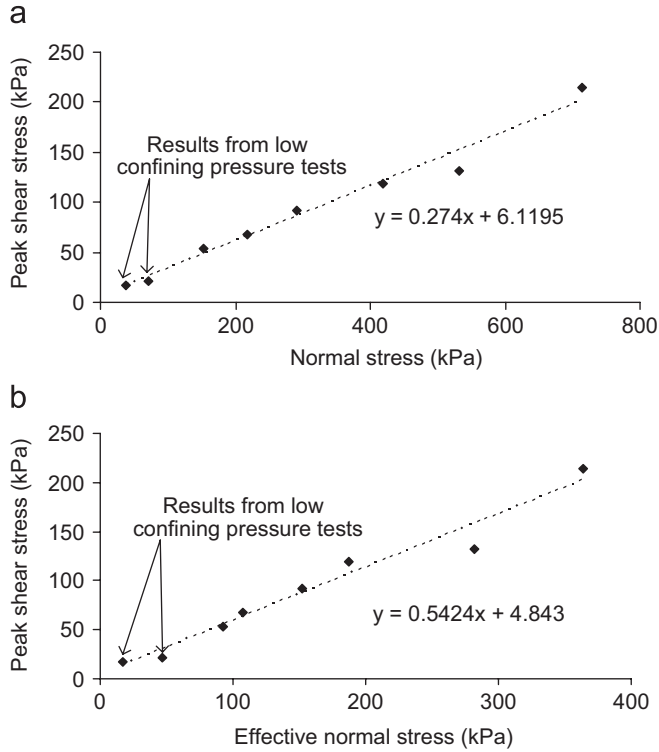


Fig. 8. Total and effective Mohr-Coulomb failure envelopes for the Tiskilwa Till.

3.3. Validation of test results

DSC validations are performed at two levels. For Level 1, predictions are compared with the test data used for finding the parameters. In Level 2, predictions are compared against the results of independent tests (i.e., tests not used for finding the parameters). Figs. 9a and b show Level 1 comparisons for typical shear tests at different confining pressures for the Tiskilwa and Sky Pilot Tills, respectively. Figs. 10a and b show Level 2 comparisons for the two tills.

Tables 5 and 6 show the parameters for evp and vevp models, respectively, for the Sky Pilot till (Sane, 2007). Fig. 11 shows typical Level 2 validation for the MDSC evp and vevp models. In Figs. 9–11 it can be seen that the finite-element predictions (Desai, 1999) made from the independent data show very good correlation with the test data.

4. Discussion

4.1. Analysis of a simulated physical system

To provide some preliminary insights into the implications of the DSC model for ice sheet motion, we present here the results of a finite-element simulation in which the DSC/HISS model is implemented (Desai, 1999) to predict

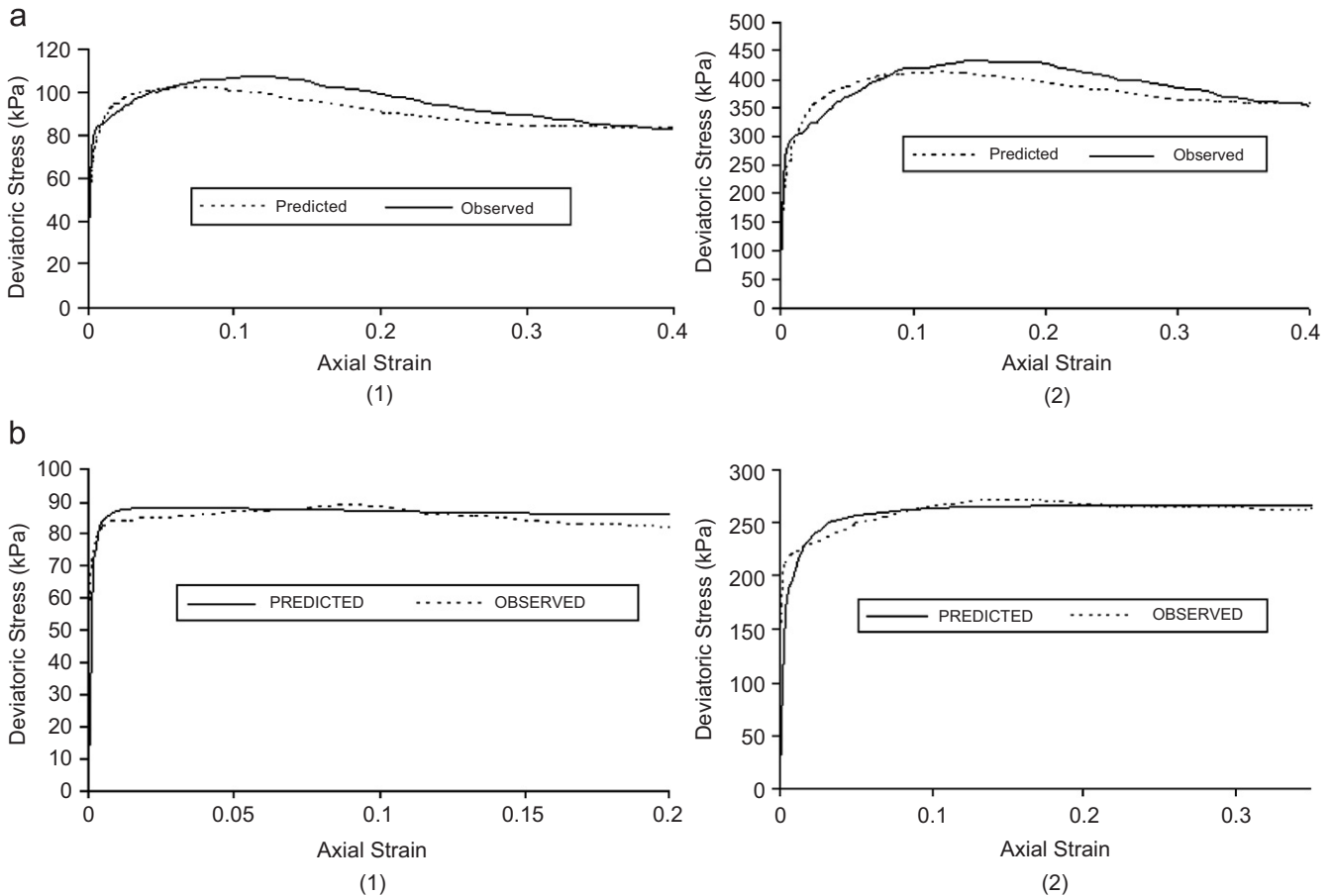


Fig. 9. (a) Level 1 back-prediction results for the Tiskilwa Till: (1) 100 kPa confining pressure; (2) 500 kPa confining pressure; (b) Level 1 back-prediction for Sky Pilot Till. (1) 100 kPa confining pressure, (2) 400 kPa confining pressure.

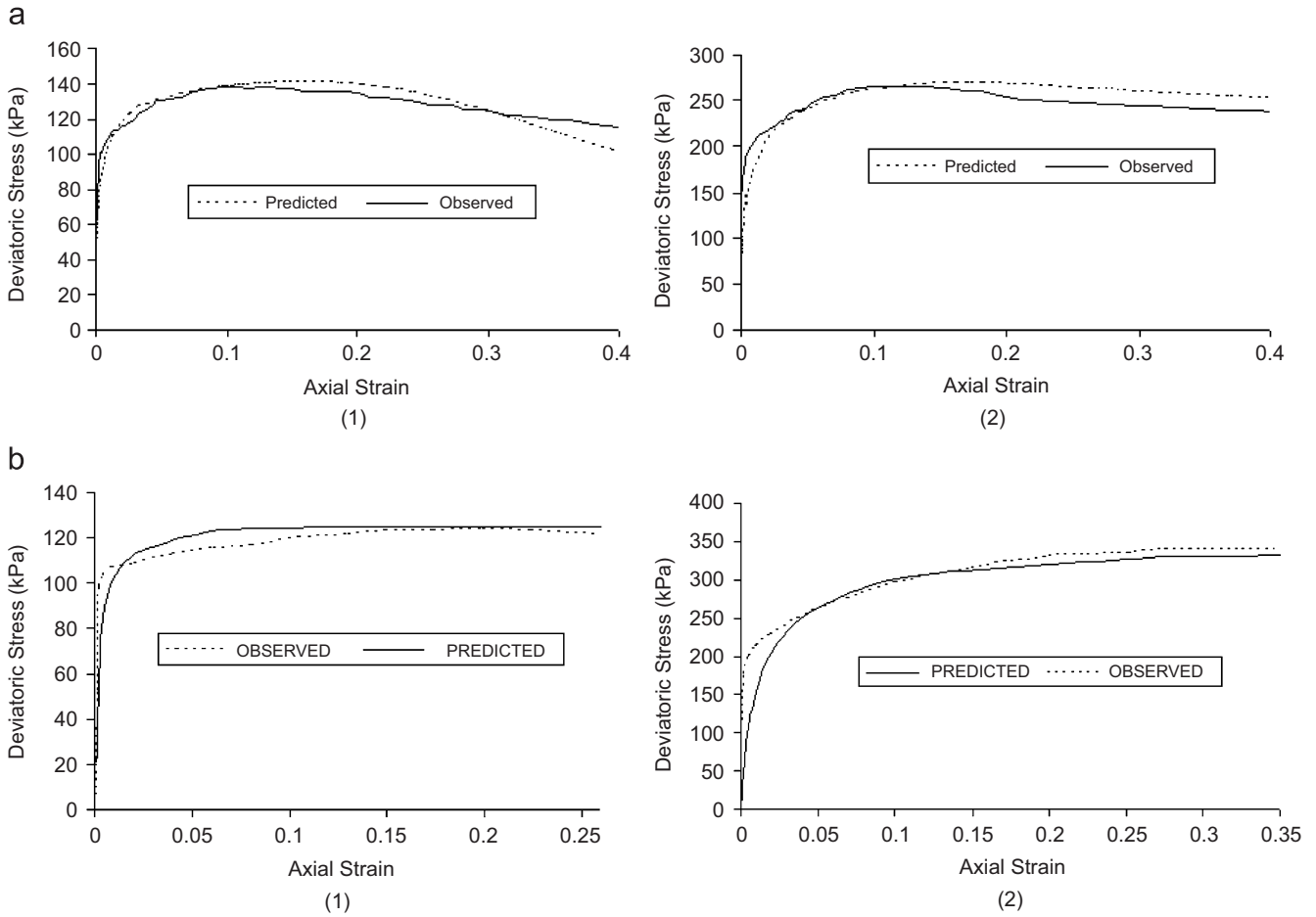


Fig. 10. (a) Level 2 back-prediction for the Tiskilwa Till: (1) 150 kPa confining pressure, (2) 400 kPa confining pressure; (b) Level 2 back-prediction for Sky Pilot Till. (1) 150 kPa confining pressure. (2) 500 kPa confining pressure.

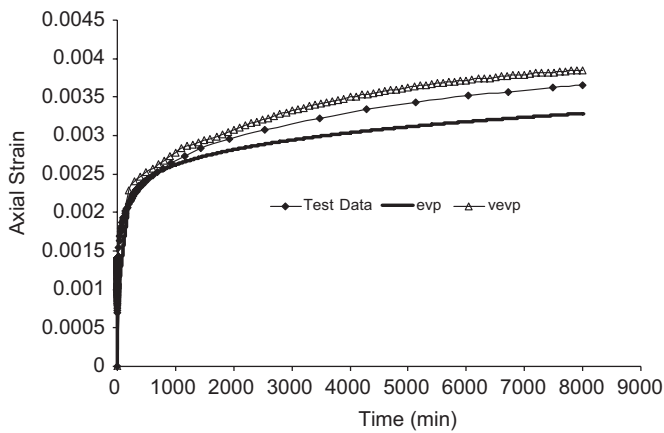


Fig. 11. Level 2 finite-element back-prediction for creep test on Sky Pilot Till for constant axial stress, $\sigma_1 = 242$ kPa, at confining stress, $\sigma_3' = 300$ kPa.

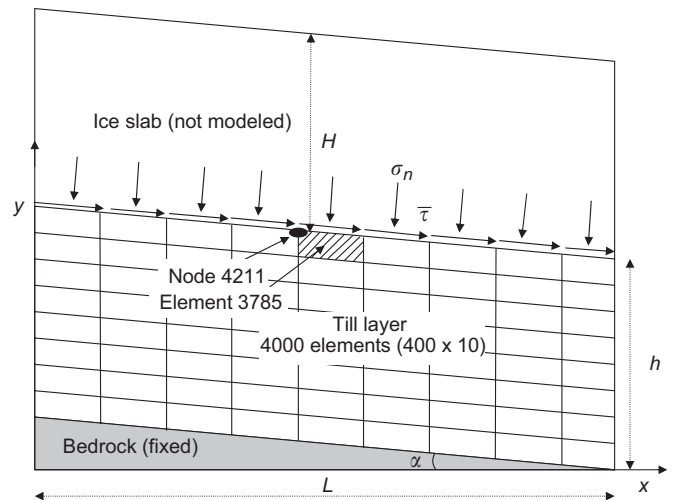


Fig. 12. Simulated section of ice slab on till and idealized finite-element mesh with loading. $L = 5000$ m. $H = 100$ m. $h = 1.5$ m (not to scale).

the motion of a 5000-m long, 100-m thick slab of ice on a 1.5-m thick layer of till lying on a 4° slope (Fig. 12). The upper and lower boundaries of the till layer are fully

coupled to the ice and bedrock, respectively. Tiskilwa Till parameters (Table 4) are assigned to the till. The finite-element program for the simulation did not include the

creep parameters, since the objective was to evaluate the failure and motion criteria rather than time-dependent behavior. Future work will incorporate time-dependent behavior as well. Two analyses, one using the DSC/HISS model with plasticity, and the second using the Mohr–Coulomb model (Table 7) are performed. In these analyses, assigned pore-water pressure is 90% of the overburden stress.

Fig. 13a shows the computed distribution of disturbance in the middle 1000-m segment (i.e., from $x = 2000$ to 3000 m of the 5000-m length) of the till layer during the incremental application of shear stress, $\bar{\tau}$, from 0 to 65 kPa. It can be seen that the disturbance grows from a very small value to greater than the critical disturbance, $D_c = 0.85$,

Table 7
Mohr–Coulomb parameters for the Tiskilwa and Sky Pilot Tills

Parameter	Tiskilwa Till	Sky Pilot Till
Total friction angle (ϕ) (deg)	15.32	13.08
Effective friction angle (ϕ') (deg)	28.47	22.31
Cohesive strength (c) (kPa)	6.11	2.18

around an applied stress, $\bar{\tau}$, of between 55 and 65 kPa. Figs. 13b and c show the variation of induced shear stress τ_{xy} (internal shear stress) developed vs. shear strain, γ_{xy} in an element at the ice–till interface at the mid-length ($x = 2500$ m) of the till layer (Fig. 12) for the DSC and Mohr–Coulomb models (Table 7), respectively. τ_{xy} , γ_{xy} , and D increase gradually with the applied shear stress. The induced shear stress, τ_{xy} , reaches a peak value at about 60 kPa in the DSC/HISS model, and then decreases. The critical disturbance, D_c , at which the failure causing the ice slab motion occurs, is observed in the post-peak zone at induced shear stress of $\tau_{xy} \approx 23$ kPa and shear strain of $\gamma_{xy} \approx 0.75$ (Figs. 13b and 14a).

On the other hand, the strains computed from the Mohr–Coulomb model are very small, and failure at the peak stress of about $\tau_{xy} \approx 62$ kPa occurs at elastic shear strain of about $\gamma_{xy} \approx 0.0048$ (Figs. 13c and 14b). Fig. 15 shows growth of horizontal displacement over the height of the till section predicted by the two models for various applied stresses. In the DSC model, displacement of about 4.5 m occurs at the applied $\bar{\tau} = 65$ kPa. On the other hand, for the Mohr–Coulomb model, failure takes place at about $\tau_{xy} = 60$ kPa (Fig. 14b) at very small shear strain

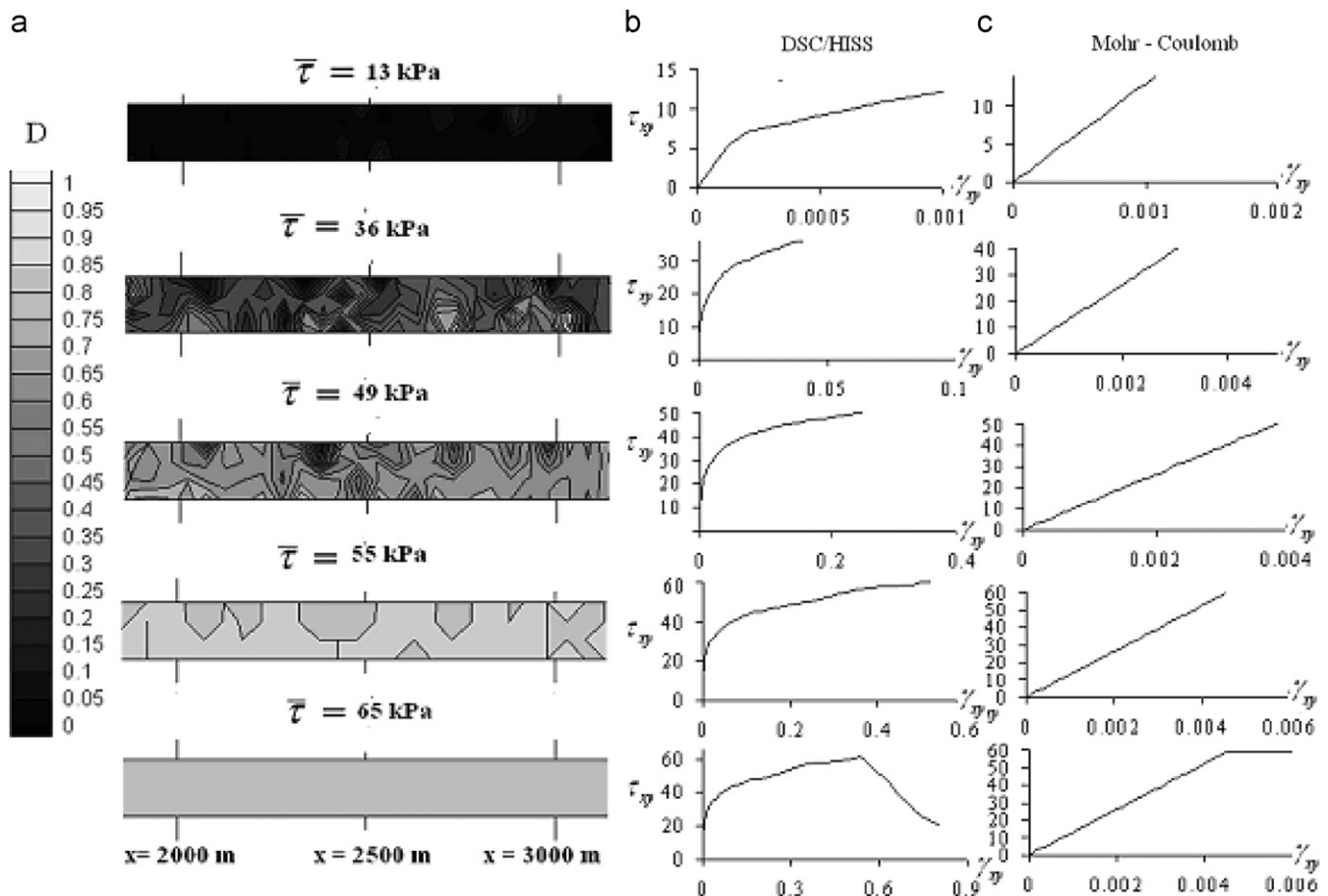


Fig. 13. (a) Predicted contours of disturbance in the central 1000-m section from DSC/HISS model at increments of external applied loading and corresponding shear stress–shear strain curves from (b) DSC/HISS model, and (c) Mohr–Coulomb model. Note differences in scale between (b) and (c).

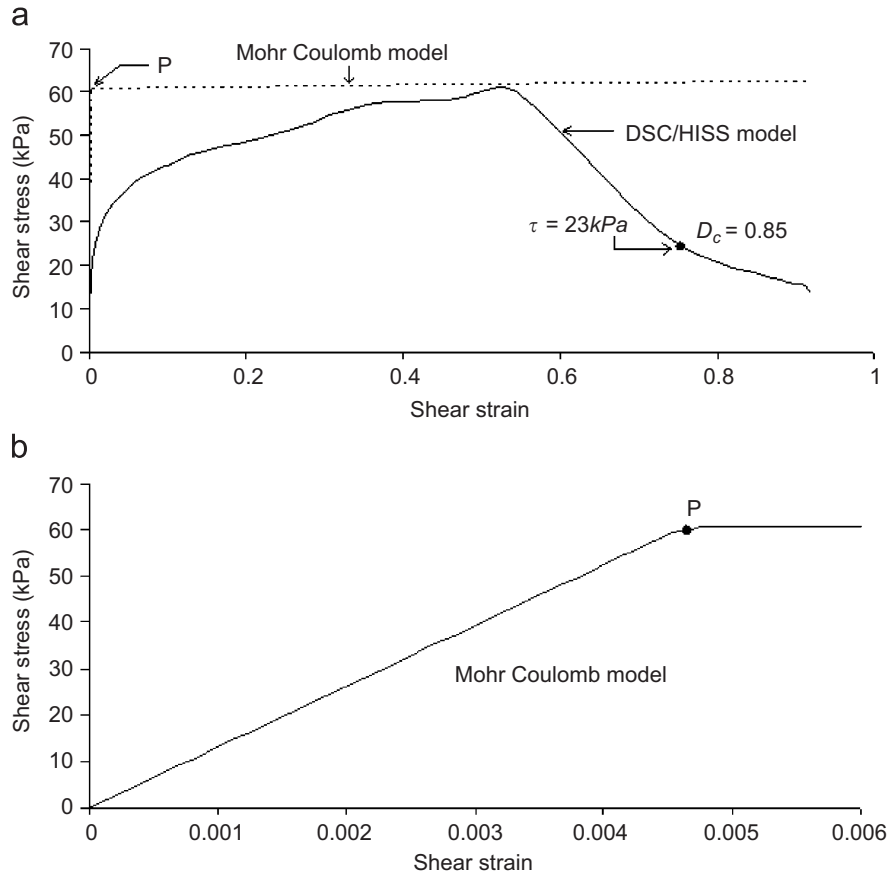


Fig. 14. Comparison between mechanism of “failure” in DSC/HISS and Mohr–Coulomb model: (a) typical stress–strain behavior with DSC/HISS model and Mohr–Coulomb model: Element no. 3745 (Fig. 12) at the interface of ice and till, in the mid-length ($x = 2500$ m) of the till layer; (b) stress–strain response from Mohr–Coulomb model in region, strain = 0–0.006. Note differences in scale between graphs (a) and (b).

($\gamma_{xy} \approx 0.0048$). Moreover, after failure (i.e., after $\gamma_{xy} \approx 0.0048$) the displacements are very large, of the order of about 16 m, i.e., catastrophic (Fig. 15b).

4.2. Comparison between the Mohr–Coulomb model and DSC/HISS model

Figs. 16a and b show the disturbance vs. total and plastic (deviatoric) strains, respectively, from a CTC test on Tiskilwa Till at $\sigma_3' = 100$ kPa. The Mohr–Coulomb model assumes that the till would deform elastically up to the peak stress (which occurs in this test at about 0.1 total strain). At the peak stress, failure should occur, inducing sudden motion to infinite strain. For the Mohr–Coulomb model, a hypothetical definition of disturbance, D , dependent on accumulated plastic strains can thus be assigned: D is 0 until at the peak stress, and after the peak stress it jumps to unity (Fig. 16a) and remains equal to unity throughout plastic strain (Fig. 16b). The test data, however, show that plastic strain (Fig. 16b) actually begins well before the peak stress is reached. It then increases as D approaches its limiting value of unity. The intersection of the tangents to the early and later parts of the disturbance curve (Fig. 16c) locates the critical disturbance, $D_c = 0.85$,

at which sufficient mass of the material has approached the FA or critical state. This compares very well with the finite-element prediction in which failure and initiation of the motion is assumed to occur at about $D_c = 0.85$ (Fig. 14a).

4.3. Proposed DSC criterion for failure and motion

Failure and resulting motion take place when $D_c \approx 0.85$, i.e., when about 85% of the total material reaches critical state. The till thus fails under a post-peak induced stress much lower than the peak stress, and at much higher strain involving considerable plastic strain. The parts in the FA (critical) state are distributed over the entire laboratory specimen (Fig. 7). We illustrate this criterion in Fig. 17. Fig. 17a shows the displacement at the finite-element node located at the ice–till interface at $x = 2500$ m (Fig. 12) vs. applied shear stress, $\bar{\tau}$. It can be seen that after the initial rise the displacement increases gradually at approximately constant rate until after the peak-induced stress of $\tau_{xy} \approx 60$ kPa. Induced shear stress then declines rapidly, and at around the point at which the induced stress $\tau_{xy} \approx 23$ kPa, and $D_c \approx 0.85$ is reached, a sudden increase in the rate of growth of displacement is observed. Fig. 17b shows the accumulated plastic strain, ξ , vs. applied axial

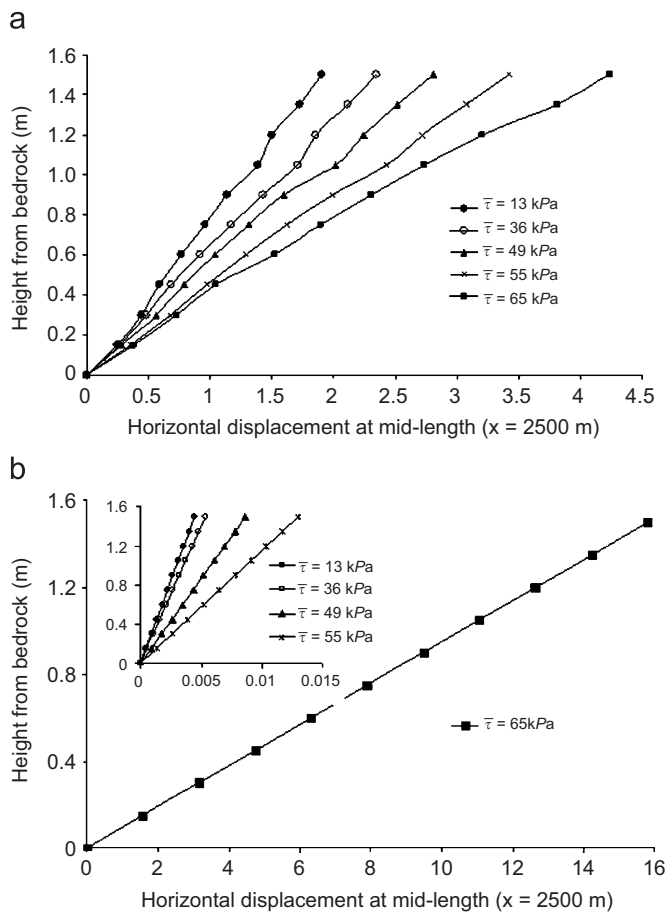


Fig. 15. Horizontal displacement at the mid-length ($x = 2500$ m) of the till layer predicted from: (a) DSC/HISS model and (b) Mohr-Coulomb model.

strain for the laboratory test data for the Tiskilwa Till at $\sigma_3' = 100$ kPa. It can be seen that at $\xi \approx 0.33$ with $D_c \approx 0.85$, the rate of increase of ξ increases. These laboratory data thus support the computer predictions from Fig. 17a. These results indicate that the failure and resulting motion occur when the entire soil mass has reached the critical condition defined by stress, strain, and the accumulated plastic strain.

5. Summary and conclusion

The DSC characterizes material deformation not only in terms of stress and strain, but also in terms of a third variable, disturbance, expressed in terms of accumulated plastic strain. It is thus a holistic model that can integrate pre-peak, peak, and post-peak behaviors into a single, unified framework from which one can predict the evolution of the behavior of the entire system. It provides a means not only for modeling behavior at the local (specimen) level, but also can be implemented numerically to predict large-scale (system) and time-dependent (including long-term) behavior. The DSC thus provides a model consistent with ideas previous put forth by others

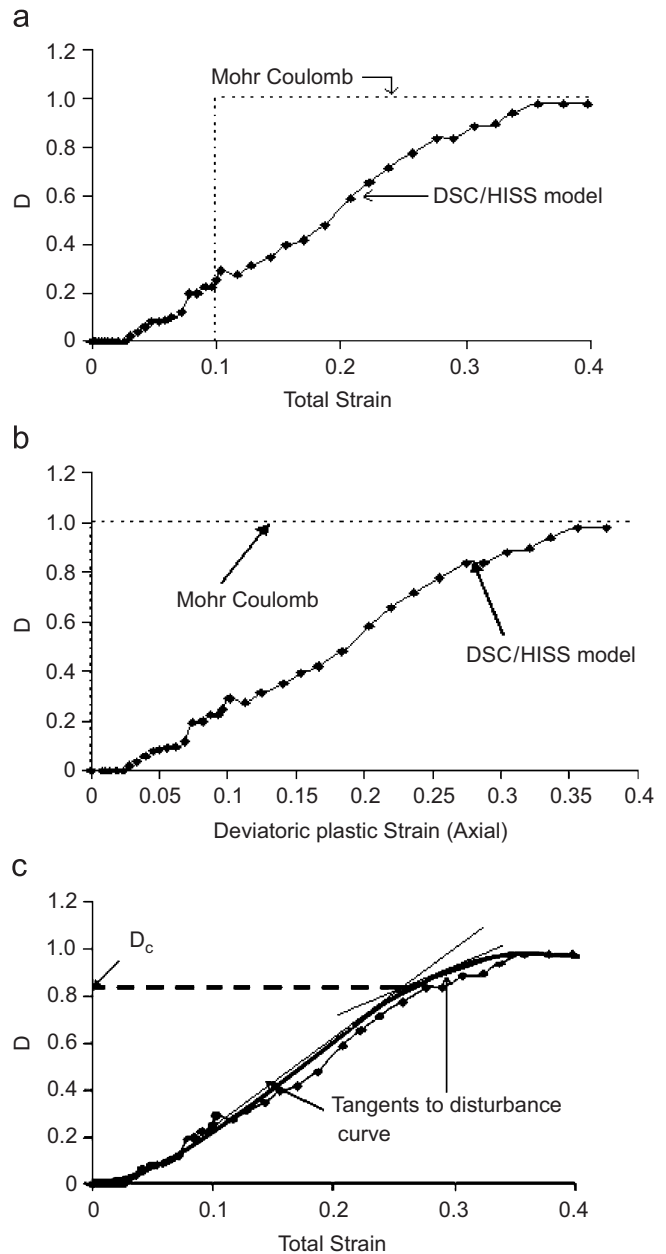


Fig. 16. Growth of disturbance for CTC test on Tiskilwa Till at $\sigma_3' = 100$ kPa: (a) disturbance vs. total strain; (b) disturbance vs. plastic strain; and (c) computation of critical disturbance, D_c .

(in particular, Hindmarsh, 1997; Piotrowski et al., 2004; Clarke 2005), as noted at the beginning of this paper.

Our simulation of a simple hypothetical coupled ice-till system, using the DSC model calibrated from comprehensive laboratory tests on a Pleistocene till, suggests that coupled ice motion should begin subsequent to the peak stress, when the till reaches critical disturbance and behavior approaches the residual state. The DSC analysis predicts that at the initiation of motion or failure, the till supports stress equal to about 20 kPa. This suggests that the till may continue to sustain a stress in the vicinity of 20 kPa after motion begins, consistent with previous observations that soils can carry a residual stress even

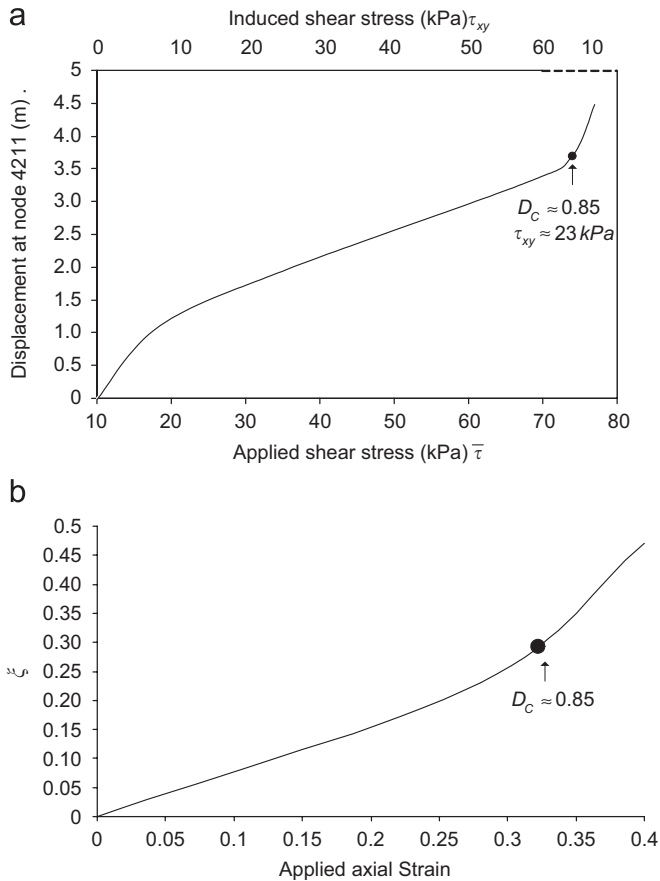


Fig. 17. (a) Variation of displacement at node 4211 (Fig. 12) vs. applied and induced stress predicted by finite-element analysis. (b) Plastic strain trajectory ξ with applied strain for CTC test on Tiskilwa Till at $\sigma'_3 = 100 \text{ kPa}$. Note: after the induced peak shear stress = 60 kPa, the induced stress reduces to about 10 kPa in the post-peak region; the variation from 60 to 10 kPa is not to scale.

after liquefaction failure under cyclic earthquake loading (Desai, 2000).

The experimental and analytical results reported in this paper demonstrate the potential of the DSC to model both local and global behavior for soft-bedded glaciers and ice sheets. We note that the DSC framework can also incorporate yet-to-be identified “sticky spot” mechanisms, and that it provides a promising means for evaluating whether and how spatially and temporally varying local conditions (cf., Fischer and Clarke, 1999) might contribute to glacier and ice sheet stability. This initial work, however, examined only the special case of complete coupling at the ice–till interface. The next step is to test and characterize the behavior of the interfaces between ice and subglacial till using the DSC model.

Acknowledgments

Funding for the project was provided by the National Science Foundation, Award no. EAR-0229513 to the University of Guam, EAR-0229889 to the University of Arizona, and EAR-0229907 to Oregon State University.

We wish to thank Ardith Hansel and Martin Roy for assistance in locating field sites and advice on field sampling, Aubri Jenson and Ramon Camacho for assistance in the field, and Arne Olsen for helpful comments on preliminary drafts of the manuscript. The paper benefited greatly from helpful reviews by Garry Clarke, Jim Rose, and an anonymous reviewer.

References

- Alley, R.B., 1989a. Water–pressure coupling of sliding and bed deformation, I: water system. *Journal of Glaciology* 35, 107–118.
- Alley, R.B., 1989b. Water–pressure coupling of sliding and bed deformation, II: velocity–depth profiles. *Journal of Glaciology* 35, 119–129.
- Alley, R.B., 1991. Deforming bed origin for southern Laurentide till sheets? *Journal of Glaciology* 37, 67–76.
- Alley, R.B., Blankenship, D.D., Bentley, C.R., Rooney, S.T., 1986. Deformation of till beneath ice stream B, West Antarctica. *Nature* 322, 57–59.
- Alley, R.B., Blankenship, D.D., Rooney, S.T., Bentley, C.R., 1987a. Till beneath Ice Stream B 4. A coupled ice–till flow model. *Journal of Geophysical Research* 95, 8931–8940.
- Alley, R.B., Blankenship, D.D., Rooney, S.T., Bentley, C.R., 1987b. Continuous till deformation beneath ice sheets. Paper presented at The Physical Basis of Ice Sheet Modelling, IAHS, Vancouver.
- Blankenship, D.D., Bentley, C.R., Rooney, S.T., Alley, R.B., 1986. Till properties beneath ice stream B. 1. Properties derived from seismic travel times. *Journal of Geophysical Research* 29, 8903–8911.
- Carlson, A.E., Jenson, J.W., Clark, P.U., 2004. Field observations from the Tiskilwa Till, IL, and Sky Pilot Till, MB of the Laurentide Ice Sheet. *Geographie Physique et Quaternaire* 58, 229–239.
- Clarke, G.K.C., 1987. Subglacial till: a physical framework for its properties and processes. *Journal of Geophysical Research* 92, 9023–9036.
- Clarke, G.K.C., 2005. Subglacial processes. *Annual Review of Earth and Planetary Science* 33, 7.1–7.30.
- DeConto, R.M., Pollard, D., 2003. Rapid Cenozoic glaciation of Antarctica induced by declining atmosphere CO_2 . *Nature* 421, 245–249.
- Desai, C.S., 1974. A consistent finite-element technique for work-softening behavior. Paper presented at International Conference on Computing Methods in Nonlinear Mechanics, University of Texas, Austin, TX.
- Desai, C.S., 1999. User Manual—DSC-SST2D, Computer code for Static, Dynamic, Creep and Thermal Analysis: Solid, Structure, and Soil—Structure Problems, Parts 1, 2 and 3, Version 2. University of Arizona, Department of Civil Engineering and Engineering Mechanics, Tucson, Arizona, USA.
- Desai, C.S., 2000. Evaluation of liquefaction using the disturbed state and energy approaches. *Journal of Geotechnical and Geoenvironmental Engineering* 126, 618–631.
- Desai, C.S., 2001. *Mechanics of Materials and Interfaces: The Disturbed State Concept*. CRC Press, Boca Raton, FL.
- Desai, C.S., Ma, Y., 1992. Modelling of joints and interfaces using the disturbed state concept. *International Journal of Numerical and Analytical Methods in Geomechanics* 16, 623–653.
- Desai, C.S., Toth, J., 1996. Disturbed state constitutive modelling based on stress–strain and nondestructive behavior. *International Journal of Solids and Structures* 33, 1619–1650.
- Desai, C.S., Somasundaram, S., Frantzikonis, G.N., 1986. A hierarchical approach for constitutive modelling of geologic materials. *International Journal of Numerical and Analytical Methods in Geomechanics* 10, 225–257.
- Desai, C.S., Samtani, N.C., Vulliet, L., 1995. Constitutive modeling and analysis of creeping slopes. *Journal of Geotechnical Engineering* 121, 43–56.

- Desai, C.S., Basaran, C., Zhang, W., 1997a. Numerical algorithms and mesh dependence in the disturbed state concept. *International Journal of Numerical Methods in Engineering* 40.
- Desai, C.S., Chia, J., Kundu, T., Prince, J., 1997b. Thermomechanical response of materials and interfaces in electronic packaging: Parts I and II. *Journal of Electronic Packaging, ASME* 119.
- Desai, C.S., Dishongh, T., Deneke, P., 1998. Disturbed state constitutive model for thermomechanical behavior of dislocated silicon with impurities. *Journal of Applied Physics* 84.
- Dredge, L.A., Nielsen, E., 1985. Glacial and interglacial deposits in the Hudson Bay lowlands: a summary of sites in Manitoba. *Current Research, Part A: Geological Survey of Canada, Paper 85-1A*, pp. 247–257.
- El Sakhway, N.R., Edil, T.B., 1996. Behavior of shaft–sand interfaces from local measurements. *Transportation Research Record* 1548, 74–80.
- Engelhardt, H., Kamb, B., 1997. Basal hydraulic system of a West Antarctic ice stream: constraints from borehole observations. *Journal of Glaciology* 43, 207–230.
- Engelhardt, H., N. Humphrey, N., Kamb, B., Fahnestock, M., 1990. Physical conditions at the base of a fast-moving Antarctic ice stream. *Science* 248, 57–59.
- Fakharian, K., Evgin, E., 2000. Elastoplastic modelling of stress-path-dependent behavior of interfaces. *International Journal of Numerical and Analytical Methods in Geomechanics* 24, 183–199.
- Fischer, U.H., Clarke, G.K.C., 1999. Evidence for temporally varying “sticky spots” at the base of Trapridge Glacier, Yukon Territory, Canada. *Journal of Glaciology* 45, 352–360.
- Geiser, F., Laloui, L., Vulliet, L., 1999. Unsaturated soil modelling with special emphasis on undrained conditions. Paper presented at 7th International Symposium on Numerical Models in Geomechanics, Balkema, Rotterdam.
- Hansel, A.K., Johnson, W.H., 1996. Wedron and Mason groups: lithostratigraphic reclassification of deposits of the Wisconsin Episode, Lake Michigan area. *Illinois State Geological Survey Bulletin* 104.
- Hindmarsh, R., 1997. Deforming Beds: Viscous and Plastic Scales of Deformation. *Quaternary Science Reviews* 16, 1039–1056.
- Humphrey, N., Kamb, B., Fahnestock, M., 1993. Characteristics of the bed of the Lower Columbia Glacier, Alaska. *Journal of Geophysical Research* 98, 837–846.
- Iverson, N.E., Iverson, R.M., 2001. Distributed shear of subglacial till due to Coulomb slip. *Journal of Glaciology* 47, 481–488.
- Iverson, N.R., 1999. Coupling between a glacier and a soft bed: II. Model results. *Journal of Glaciology* 45, 41–53.
- Iverson, N.R., Hooyer, T.S., Baker, R.W., 1998. Ring-shear studies of till deformation: Coulomb-plastic behavior and distributed strain in glacier beds. *Journal of Glaciology* 44, 634–642.
- Iverson, N.R., Baker, R.W., Hooke, R.L., Hanson, B., Jansson, P., 1999. Coupling between a glacier and a soft bed: I. A relation between effective pressure and local stress determined from till elasticity. *Journal of Glaciology* 45, 31–40.
- Jenson, J.W., MacAyeal, D.R., Clark, P.U., Ho, C.L., Vela, J.C., 1996. Numerical modeling of subglacial sediment deformation: implications for the behavior of the Lake Michigan Lobe, Laurentide Ice Sheet. *Journal of Geophysical Research* 101, 8717–8728.
- Johnson, W.H., Hansel, A.K., 1990. Multiple Wisconsinan glacial sequences at Wedron, Illinois. *Journal of Sedimentary Petrology* 60, 26–41.
- Johnson, W.H., Hansel, A.K., 1999. Wisconsin Episode glacial landscape of central Illinois: a product of subglacial deformation process? *Geological Society of America Special Paper* 337, 121–135.
- Kamb, B., 1991. Rheological nonlinearity and flow instability in the deforming bed mechanism of ice stream motion. *Journal of Geophysical Research* 96, 585, 516,595.
- Kamb, B., 2001. Basal zone of the West Antarctic ice streams and its role in lubrication of the rapid motion. *The West Antarctic Ice Sheet: behavior and environment. Antarctic Research Series* 77, 157–199.
- Kavanaugh, J.L., Clarke, G.K.C., 2006. Discrimination of the flow law for subglacial sediment using in situ measurements and an interpretation model. *Journal of Geophysical Research* 111, F01002.
- Klassen, R.W., 1986. Surficial geology of the north-central Manitoba. *Geological Survey of Canada Memoir* 419, 57.
- Lambe, T.W., Whitman, R.V., 1969. *Soil Mechanics*. Wiley, New York, USA.
- Lupini, J.F., Skinner, A.E., Vaughan, P.R., 1981. The drained residual strength of cohesive soils. *Geotechnique* 31, 181–213.
- MacAyeal, D.R., 1989. Large-scale ice flow over viscous basal sediment: theory and application to Ice Stream B, Antarctica. *Journal of Geophysical Research* 94, 16585–16595.
- Mickelson, D.M., Clayton, L., Fullerton, D.S., Borns Jr., H.W., 1983. The Late Wisconsin glacial record of the Laurentide Ice Sheet in the United States. In: Wright, Jr., H.E. (Ed.), *Late-Quaternary Environments of the United States*. University of Minnesota Press, Minneapolis, pp. 3–37.
- Muir-Wood, D., 1990. *Soil Behaviour and Critical State Soil Mechanics*. Cambridge University Press, Cambridge, 462pp.
- Nielsen, E., Morgan, A.V., Morgan, A., Mott, R.J., Rutter, N.W., Causse, C., 1986. Stratigraphy, paleoecology, and glacial history of the Gillam area, Manitoba. *Canadian Journal of Earth Sciences* 23, 1641–1661.
- Pal, S., Wathugala, G.W., 1999. Disturbed state model for sand-geosynthetic interfaces and application. *International Journal of Numerical and Analytical Methods in Geomechanics* 23, 1873–1892.
- Pande, G.N., Owen, D.J.R., Zienkiewicz, O.C., 1997. Overlay models in time-dependent non-linear material analysis. *Computers and Structures* 7, 435–443.
- Pandey, A., 2005. Disturbed state modelling for creep response of subglacial till. M.S. Thesis, Department of Civil Engineering and Engineering Mechanics, University of Arizona, Tucson, Arizona, USA.
- Piotrowski, J.A., Mickelson, D.M., Tulaczyk, S., Krzyskowski, D., Junge, F.W., 2001. Were deforming subglacial beds beneath past ice sheets really widespread? *Quaternary International* 86, 139–150.
- Piotrowski, J.A., Larsen, N.K., Junge, F.W., 2004. Reflections on soft subglacial beds as a mosaic of deforming and stable spots. *Quaternary Science Reviews* 23, 993–1000.
- Prochazka, P.P., Trckova, J., 2000. Coupled modeling using DSC and TFA Theoretical Process. Paper presented at 10th International Conference on Computer Methods and Advances in Geomechanics, Balkema.
- Roscoe, K.H., Schofield, A.N., Wroth, C.P., 1958. On the yielding of soils. *Geotechnique* 8, 22–52.
- Roy, M., 1998. Pleistocene stratigraphy of the lower Nelson River area-implications for the evolution of the Hudson Bay lowland of Manitoba, Canada. M.S. Thesis, University of Quebec, Montreal, 220pp.
- Sane, S.M., 2007. Disturbed state concept based constitutive modeling for reliability analysis of lead free solders electronic packaging, and for prediction of glacial motion. Ph.D. Thesis, University of Arizona, Tucson.
- Skempton, A.W., 1985. Residual strength of clays in landslides, folded strata, and the laboratory. *Geotechnique* 14, 75–101.
- Tarasov, L., Peltier, W.R., 2004. A geophysically constrained large ensemble analysis of the deglacial history of the North American ice-sheet complex. *Quaternary Science Reviews* 23, 359–388.
- Thorleifson, L.H., Wyatt, P.H., Shilts, W.W., Nielsen, E. (Eds.), 1992. *Hudson Bay Lowland Quaternary Stratigraphy: Evidence for Early Wisconsinan Glaciation Centered in Quebec*. Geological Society of America, pp. 207–222.
- Tulaczyk, S., 1999. Ice sliding over weak, fine-grained tills: dependence of ice–till interactions on till granulometry. In: Mickelson, D.M., Attig, J.W. (Eds.), *Glacial Processes: Past and Present*. Geological Society of America, pp. 159–177.
- Tulaczyk, S., Kamb, W.B., Engelhardt, H.F., 2000a. Basal mechanics of Ice Stream B, West Antarctica 2. Undrained plastic bed model. *Journal of Geophysical Research* 105, 483–494.

- Tulaczyk, S., Kamb, W.B., Engelhardt, H.F., 2000b. Basal mechanics of Ice Stream B, West Antarctica I. Till mechanics. *Journal of Geophysical Research* 105, 463–481.
- Varadarajan, A., Sharma, K.G., 2000. Constitutive modeling and determination of parameters for rock mass and rock fill materials. Paper presented at 10th International Conference on Computer Methods and Advances in Geomechanics, Balkema.
- Varadarajan, A., Sharma, K.G., Soni, M., 1999. Constitutive modeling of a reinforced soil using the hierarchical model. *International Journal of Numerical and Analytical Methods in Geomechanics* 23, 217–241.
- Vulliet, L., Laloui, L., 2000. Unsaturated Soil Mechanics: Constitutive Modeling and Coupling Effects. Paper presented at 10th International Conference on Computer Methods and Advances in Geomechanics, Balkema.
- Wickham, S.S., Johnson, W.H., 1981. The Tiskilwa Till: a regional view of its origin and depositional processes. *Annals of Glaciology* 2, 176–182.